Modeling and Optimal Modulation of MAB Converter Using Full-Order Impedance Matrix

Chanaka Singhabahu, *Member, IEEE*, Ayooluwa Ajiboye, *Student Member, IEEE*, Rakesh Resalayyan, *Member, IEEE*, Akshay Singh, *Member, IEEE*, Arafat Hasnain, *Student Member, IEEE*, and Alireza Khaligh, *Senior Member, IEEE*

***Abstract*—Multiactive-bridge (MAB) converter is gaining high interest as a multiport converter topology due to its multidirectional power flow capability, zero voltage switching, and galvanic isolation between ports with voltage step-up/down. One of the key components of the MAB converter is the high-frequency n-port magnetic link. An $n \times n$ impedance matrix is a full order model to represent an n -port passive network, without losing any information seen from the ports. In this work, a full-order impedance matrix-based model for an MAB converter is introduced, and a systematic approach is devised to find the optimal modulation parameters which minimize the converter losses. This approach is deployed to obtain desired power flow, minimize conduction losses, and analyze zero-voltage-switching (ZVS) conditions. A frequency domain model is developed which uses the impedance matrix to solve for the branch currents. The inductance matrix of the high-frequency ac link is further used with the frequency domain model to analyze the port ZVS conditions by investigating the inductive energy in the high frequency ac link. The work is experimentally verified on a GaN based four-port 250-W MAB converter with its ports rated at 200 V, 30 V, 16 V, and 8 V.**

***Index Terms*—Conduction loss estimation, frequency domain modeling, full-order inductance matrix, multiactive-bridge (MAB) converter, optimal modulation, zero-voltage-switching (ZVS) modeling.**

I. Introduction

THE multiactive-bridge (MAB) converter is a versatile multiport converter topology which is capable of providing multidirectional power flow using a coupled n-port magnetic link. Derived from the well-established dual active bridge (DAB) converter [1], [2], [3], this topology provides benefits including zero-voltage-switching (ZVS), low component count and scalability to large number of ports. Due to these advantages, especially enabled by the use of wide-bandgap devices, there has been a increased adoption of MAB derived topologies in a multitude of applications including smart home energy routers [4], solid-state-transformers [5], [6], electric vehicle onboard chargers [7], battery management systems [8], and more electric aircraft power distribution systems [9]. Due to the elimination of intermediate conversion stages, the MAB converter has been investigated as a suitable candidate in applications with local energy generation and storage [10], [11], [12]. By enabling direct power flow among ports, additional losses incurred in typical two-stage systems are alleviated leading to improved efficiency [5].

To control the power flow between the ports, single phase shift (SPS) control has been primarily used due to its simplicity and availability of closed-form equations for power transfer and RMS currents [13], [14], [15]. However, the major drawback in SPS control is the large circulating current in the ac link when operating at nonunity reflected voltage gains [16], [17]. To improve on this issue, based on Triple Phase Shift control in DAB converters, the duty-ratio are used as additional control variables to optimize for conduction losses in MAB converters [7].

Another key element in a MAB converter is the high frequency magnetic structure (which is comprised of multiwinding transformer and branch inductors) used for coupling the ports of the converter. Modeling of these magnetics plays a key role in obtaining optimal modulation variables. In [17], star model was used to represent the magnetic structure. While allowing for a simplified analysis, these reduced order models rely on assumptions of certain cross-coupling terms to be negligible, and thus fail to fully capture the coupling relationships in multiport magnetic links with complex magnetic designs [18]. For example, the magnetic coupling in asymmetric-leakage integrated multiport transformers, where the leakage energy is used to integrate the series branch inductors, cannot be fully represented using such models [19], [20]. Nevertheless, even in the case without any leakage integration, it is common to have complex magnetic structures that create coupling relationships that deviate from the assumptions made to represent using a reduced order model [21]. In such cases, if the MAB converter is modeled with a reduced order model, discrepancies arise, resulting in substantial deviations from the desired operating point. This results in inaccuracies in the resultant port power levels, loss of ZVS operation, and suboptimal modulation parameters which in turn lead to increased converter losses. The authors in [20] and [22] presented a full-order $n \times n$ inductance and resistance matrix, capturing all the coupling relationships in an

Manuscript received 21 August 2023; revised 4 February 2024 and 4 June 2024; accepted 5 August 2024. Date of publication 12 August 2024; date of current version 11 September 2024. This work was supported in part by Maryland Energy Innovation Institute (MEI^2). Recommended for publication by Associate Editor Z. Li. *(Corresponding author: Chanaka Singhabahu.)*

The authors are with the Maryland Power Electronics Laboratory, Department of Electrical and Computer Engineering, Institute for Systems Research, University of Maryland, College Park, MD 20742 USA (e-mail: chanaka@terpmail.umd.edu; ajiboye1@umd.edu; rakeshr@ieee.org; aksingh@umd.edu; hasnain@umd.edu; khaligh@umd.edu).

Color versions of one or more figures in this article are available at https://doi.org/10.1109/TPEL.2024.3442009.

Digital Object Identifier 10.1109/TPEL.2024.3442009

n-port network, which will be effectively utilized in this work for obtaining the optimal modulation parameters.

For MAB converters with a higher number of ports, with the introduction of duty-ratio control, the number of operating modes increase dramatically. Modeling an MAB converter using time-domain approach prevalent in DABs [23], can complicate the overall analysis to achieve the optimal modulation variables due to the increased number of operating modes. In [7] and [24], generalized harmonic approximation-based frequency domain modeling approach was used to find optimal modulation parameters in an MAB converter. Even though the above methods utilized the duty-ratio variables for control, the objective function to find optimal modulation parameters was based on the squared RMS currents or minimization of reactive power which was used as a proxy for conduction losses. While such methods would work for a symmetric design with nearly equal specifications for all the ports, it would lead to suboptimal results when used in a more sophisticated design with asymmetric port voltage/power specifications. Furthermore, in [7], the investigation of ZVS conditions were performed by identifying the direction of current, which did not guarantee ZVS transition based on the energy requirements [25], [26]. A detailed ZVS analysis of the modular three-port MAB converter topology was presented in [27] by using time domain mode-wise analysis. This method only utilized SPS control, which would limit the performance, especially at operating points with a nonunity-gain for the reflected voltages from each port. Due to the large number of operating modes involved in time domain analysis, the method is not easily extendable for an MAB with increased number of ports. In [17], the authors presented a multivariable modulation strategy for an n-port MAB converter. The ZVS conditions are evaluated using a Thevenin equivalent circuit for the star-model of the transformer. As explained later in this article, since the star-model being a reduced-order model, it fails to capture all coupling relationships in multiwinding transformer structures [18]. Furthermore, the loss optimization algorithm uses proxy variables to model the conduction and switching losses [17], which do not accurately capture the complex branch current dependent loss mechanisms in multiwinding transformers [21], [22].

In summary, the key limitation in the modeling methods in the existing literature is the analysis of the MAB with its magnetic link represented using reduced-order models (e.g., star model). In such cases, if the MAB converter is modeled with a reduced order model, discrepancies arise, resulting in substantial deviations from the desired operating point. This results in inaccuracies in the resultant port power levels, loss of ZVS operation, and suboptimal modulation parameters which in turn lead to increased converter losses. To address these limitations, the following are the key contributions of this article.

1) A generalized n-port frequency domain modeling approach which utilizes the $n \times n$ impedance matrix of the ac link to obtain optimal modulation parameters of the MAB converter. The use of frequency domain modeling instead of time domain modeling provides a unified method to integrate the large number of phase-shift and duty ratio variables into a single framework without the need for mode-wise analysis. As the impedance matrix-based modeling approach allows to completely model the n-port passive network, it is able to accurately capture the magnetic coupling and hence the power flow in MAB converter.
2) A port equivalent inductance and equivalent reflected voltage based on the full-order inductance matrix of the magnetic link, which is subsequently used to develop the ZVS criterion. This enables accurate representation of the equivalent inductance seen by the port to simplify the ZVS analysis of an MAB converter to well-established DAB converter. Furthermore, the model is directly compatible with results obtained from finite-element-analysis (FEA) tools, allowing it to evaluate complex magnetic shapes designed for MAB converters in a practical design flow.
3) In addition to the inductance matrix, the resistance matrix of the n-port network is also incorporated into the proposed impedance matrix based model to further improve the modeling accuracy and capture loss mechanisms that are distinctive to multiwinding transformers. The optimal modulation parameters obtained using the proposed method ensure that the MAB converter operates in the desired operating point in terms of power flow, while reducing the conduction loss and enhancing the ZVS performance, compared to the existing methods.

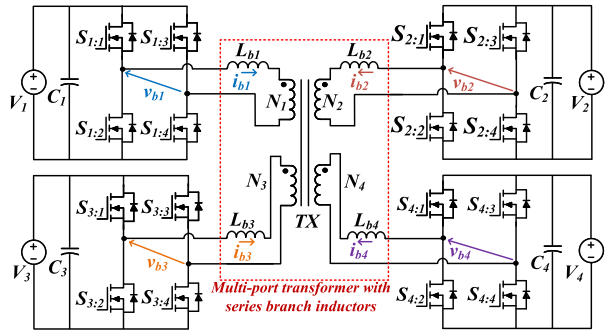

Fig. 1. MAB converter topology with each port configured as full-bridge.

The rest of this article is organized as follows. Section II introduces the impedance matrix-based modeling method for MAB converter. In Section III, a systematic algorithm to find optimal modulation parameters for a given operating point is presented. The proposed model is validated through simulations and experiments in Section IV. Finally, Section V concludes this article.

II. Proposed MAB Converter Model

In this section, the formation of ac link impedance matrix and the proposed methodology to derive the branch currents, power transfer and other quantities will be discussed. To define the circuit parameters, the four-port MAB converter topology shown in Fig. 1 is considered. The circuit topology is comprised of four dc ports, with voltages V_1, V_2, V_3, and V_4. Each port is connected to a full-bridge circuit, where each bridge leg is switched at a frequency of f_{sw} with complementary switching

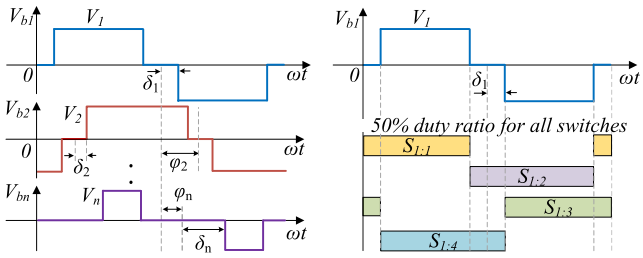

Fig. 2. Modulation variables in MAB converter with phase shift modulation.

logic having 50% duty ratio. As illustrated in Fig. 2, by using the modulation parameters $\delta_{\rm i}$ and $\varphi_{\rm i}$ (where i is the port index), the duty-ratio and phase shift (w.r.t. port 1) of the quasi-square wave branch voltage ($v_{\rm bi}$) is controlled, respectively. The high-frequency inverting terminals of each full bridge is interfaced with the high frequency magnetic link which is comprised of a four-port transformer (TX) and external series branch inductors ($L_{\rm bi}$).

A. Impedance Matrix Representation of MAB AC Link

Without the loss of any magnetic coupling information, a four-port transformer can be represented using a 4×4 inductance matrix [18]. In addition to the transformer, if external branch inductors are connected to each transformer port as shown in Fig. 1, they are directly added to the diagonal terms in the transformer inductance matrix, thereby modeling the entire magnetic link using a single inductance matrix ($\mathbf{L}$) as given in (1), where l_{ii} refers to the self inductance term of each transformer port and $l_{ij}; i \neq j$ are the mutual inductance terms in the multiport transformer [18]. The inductance matrix of a multiport transformer can be obtained by using several methods, including FEA simulations or experimental measurements as discussed in [20].

$$\mathbf{L} = \begin{bmatrix} l_{11}+L_{b1} & l_{12} & l_{13} & l_{14} \\ l_{21} & l_{22}+L_{b2} & l_{23} & l_{24} \\ l_{31} & l_{32} & l_{33}+L_{b3} & l_{34} \\ l_{41} & l_{42} & L_{43} & l_{44}+L_{b4} \end{bmatrix}. \quad (1)$$

In addition to the inductive properties in the high frequency link, it is vital to model the resistances introduced by the transformer, branch inductors, and the semiconductor switches. At high frequency operation, the magnitude and phase of respective branch currents in the transformer affect the effective ac resistance in a multiport transformer [21]. Therefore, it is inaccurate to use only a series resistance term to model the ac resistance of each transformer port, which does not capture the dependency on port current. To address this, this work uses the resistance matrix of the transformer [22], thereby enabling accurate modeling of transformer losses in the MAB converter. It should be noted that the elements in the resistance matrix are frequency dependent, and can be extracted using an FEA simulation of the transformer. In addition to the transformer, resistances of the series branch inductors (R^i_{Lb}) and the ON-state resistance of series switches in the conduction path ($R^i_{ds,\rm total}$) are directly included in the diagonal terms of the final resistance matrix ($\mathbf{R}$), where $R_{\rm bi} = R^i_{Lb} + R^i_{ds,\rm total}$ and i is the port index. For a full-bridge as there are always two switches in the conduction path of the branch current, $R^i_{ds,\rm total}$ is twice the ON-state resistance of individual switch ($R_{ds,\rm on}$), (i.e., $R^i_{ds,\rm total} = 2R^i_{ds,\rm on}$). While for a half-bridge, since there is only one series conducting switch, $R^i_{ds,\rm total} = R^i_{ds,\rm on}$. It should be noted that while the switch resistances are modeled as constant values in this work, the presented framework allows for these resistances to be further parameterized as a function of temperature, drain currents, and gate voltages.

$$\mathbf{R}(\omega) = \begin{bmatrix} r_{11}+R_{b1} & r_{12} & r_{13} & r_{14} \\ r_{21} & r_{22}+R_{b2} & r_{23} & r_{24} \\ r_{31} & r_{32} & r_{33}+R_{b3} & r_{34} \\ r_{41} & r_{42} & r_{43} & r_{44}+R_{b4} \end{bmatrix}. \quad (2)$$

The resistive and the inductive elements of the MAB high-frequency link are combined to create the effective impedance matrix, $\mathbf{Z}(\omega)$ as given in (3). Here, $\omega = 2\pi k f$, where f is the frequency of sinusoidal excitation.

$$\mathbf{Z}(\omega) = j\omega\mathbf{L} + \mathbf{R}(\omega). \quad (3)$$

B. Generalized Harmonic Approximation

As illustrated in Fig. 2, the branch voltages are quasi-square wave shapes composed of multiple frequency components. However, the impedance matrix in (3) is defined for a single frequency. Therefore, to analyze how the ac link behaves for a quasi-square voltage waveform, the branch voltages are decomposed into corresponding harmonic components using Fourier analysis. The branch voltage can be written as a superposition of multiple harmonics (4), where V_i is the port voltage of ith port, $\overrightarrow{V_{{\rm bi},k}}$ is the kth harmonic coefficient of branch voltage as given in (5). Also, h_i takes a value of 2 or 1 depending on whether a half bridge converter or a full-bridge converter is connected to the ith port, respectively. Here, $\omega_{\rm sw} = 2\pi f_{\rm sw}$ and $H_{\max}$ refers to the number of harmonic components used in superposition.

$$v_{\rm bi}(t) = \sum_{\substack{m=0 \\ k=2m+1}}^{H_{\max}} \left|\overrightarrow{V_{{\rm bi},k}}\right| \sin\left(k\omega_{\rm sw}t + \angle\overrightarrow{V_{{\rm bi},k}}\right) \quad (4)$$

$$\overrightarrow{V_{{\rm bi},k}} = \frac{4V_i}{kh_i\pi}\cos\left(k\delta_{\rm i}\right)e^{-jk\varphi_{\rm i}}. \quad (5)$$

The relationship between branch voltages and branch currents can be expressed as (6) by using the impedance matrix for kth harmonic component, where $\mathbf{V_k} = [\overrightarrow{V_{b1,k}}\ \overrightarrow{V_{b2,k}}\ \overrightarrow{V_{b3,k}}\ \overrightarrow{V_{b4,k}}]^T$, $\mathbf{I_k} = [\overrightarrow{I_{b1,k}}\ \overrightarrow{I_{b2,k}}\ \overrightarrow{I_{b3,k}}\ \overrightarrow{I_{b4,k}}]^T$, and $\mathbf{Z_k} = \mathbf{Z}(k\omega_{\rm sw})$

$$\mathbf{V_k} = \mathbf{Z_k}\mathbf{I_k}. \quad (6)$$

Fourier series coefficient corresponding to kth harmonic of branch current ($\overrightarrow{I_{{\rm bi},k}}$) is obtained by solving (6) for $\mathbf{I_k}$ using matrix inverse operation as shown in (7)

$$\mathbf{I_k} = \mathbf{Z_k^{-1}}\mathbf{V_k}. \quad (7)$$

The harmonic components of branch currents obtained in (7) are superimposed as shown in (8) to obtain the time-domain reconstruction of the branch current.

$$i_{\text{bi}}(t) = \sum_{\substack{m=0 \\ k=2m+1}}^{H_{\max}} \left|\overrightarrow{I_{\text{bi},k}}\right| \sin\left(k\omega_{\text{sw}}t + \angle\overrightarrow{I_{\text{bi},k}}\right). \tag{8}$$

Furthermore, by using the Fourier series coefficients of branch voltage and currents, important circuit quantities (port power, port RMS current, and conduction loss) can be obtained in frequency domain.

The switch ON-resistance and track resistances comes in series with the current path, and hence are added to the diagonal terms of the **R** matrix. Since the effect of ON-resistance of the switches is modeled, the switches can be considered lossless and the power seen on the high frequency bridge port is same as the power seen on the dc side. Therefore, the active port power of the MAB converter is expressed using the following:

$$P_i = \sum_{\substack{m=0 \\ k=2m+1}}^{H_{\max}} \frac{1}{2}\mathfrak{Re}(\overrightarrow{V_{\text{bi},k}} \cdot \overrightarrow{I_{\text{bi},k}}^{*}). \tag{9}$$

With this information, the switching cycle average load current (I_i) taken from (or supplied to) each port can be expressed as

$$I_i = \frac{P_i}{V_i} = \frac{1}{V_i} \sum_{\substack{m=0 \\ k=2m+1}}^{H_{\max}} \frac{1}{2}\mathfrak{Re}(\overrightarrow{V_{\text{bi},k}} \cdot \overrightarrow{I_{\text{bi},k}}^{*}). \tag{10}$$

Moreover, the port RMS current is written as follows:

$$i_{\text{bi,rms}} = \sqrt{\sum_{\substack{m=0 \\ k=2m+1}}^{H_{\max}} \frac{1}{2}(\overrightarrow{I_{\text{bi},k}} \cdot \overrightarrow{I_{\text{bi},k}}^{*})}. \tag{11}$$

With the resistance matrix already defined in (2), an expression for the conduction losses (P_{cond}) can be written as follows:

$$P_{\text{cond}} = \sum_{\substack{m=0 \\ k=2m+1}}^{H_{\max}} \frac{1}{2}\mathbf{I_k^T R_k I_k^*} \tag{12}$$

where $\mathbf{R_k} = \mathbf{R}(k\omega_{\text{sw}})$ is the resistance matrix corresponding to the kth harmonic.

C. DAB Equivalent Representation of MAB Port

A key benefit of the DAB and MAB topology family is the possibility of achieving ZVS switching across wide operating range, resulting in substantially lower switching losses. The analysis of ZVS conditions for DAB converters has been well-investigated in literature [25], [26], [28]. As derived in [25] for a DAB converter, the sufficient condition for ZVS of a particular port depends on the branch current direction, current magnitude, branch voltage, effective series inductance (also referred to as the leakage inductance), and the reflected branch voltage from the other port. While obtaining the reflected voltage and total series inductance is straightforward for a DAB converter, this is not the case for the MAB converter due to the complex magnetic coupling.

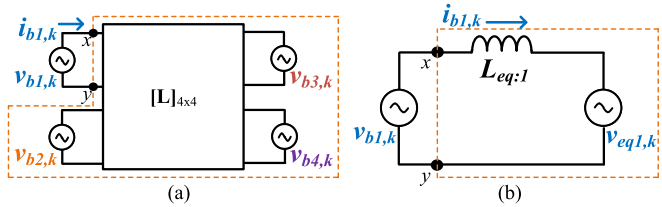

Fig. 3. DAB equivalent representation of port 1 of MAB converter.

To accurately investigate the ZVS transition of the jth port of the MAB converter, it is required to obtain the equivalent reflected voltage from all the other ports ($V_{eq:j}$) as well as the equivalent series inductance ($L_{eq:j}$). Due to the increased number of ports as well as modulation parameters in the MAB converter topology, a large number of operating modes exist. By using the impedance matrix based MAB converter model introduced above, a unified method to obtain $V_{eq:j}$ and $L_{eq:j}$ is presented hereinafter.

In this work, the objective is to simplify the MAB port which needs to be analyzed as a DAB converter configuration. This enables the use of existing knowledge base for DAB ZVS analysis for the case of MAB converter. For the purpose of ZVS analysis, only the inductive energy in the ac link is considered by setting $\mathbf{R_k} = [0]$, simplifying $\mathbf{Z}_k$ as follows:

$$\mathbf{Z}_k = jk\omega_{\text{sw}}\mathbf{L}. \tag{13}$$

Without loss of generality, port 1 is used as the reference, to derive the expressions for $\overrightarrow{V_{eq:1,k}}$ and $L_{eq:1}$. As discussed before, the inductance matrix is a physical property of the high frequency ac link and does not depend on the voltages applied by each port. It can be noted that $\overrightarrow{V_{b1,k}}$ in Fig. 3(b) is generated by the switching action of the full bridge circuit in port 1, while $v_{eq:1,k}$ is generated by the combined effect of voltages applied from other ports. Hence, by equating all the branch voltages other than that of the port 1 to zero, makes $\overrightarrow{V_{eq:1,k}} = 0$ in Fig. 3(b). The port 1 current, $\overrightarrow{I_{b1,k}}$, corresponding to scenario can be equated in two ways to solve for $L_{eq:1}$: 1) from Fig. 3(b) as given in (14); 2) by using (7) and (13) by substituting $\overrightarrow{V_{\text{bi},k}} = 0$ (where $i = \{2, 3, 4\}$) as given as follows, where $[\mathbf{L^{-1}}]_{(w,v)}$ is the element in row w and column v of the inverse inductance matrix:

$$\overrightarrow{I_{b1,k}} = \frac{\overrightarrow{V_{b1,k}}}{jk\omega_{\text{sw}}L_{eq:1}} \tag{14}$$

$$\overrightarrow{I_{b1,k}} = \frac{[\mathbf{L^{-1}}]_{(1,1)}}{jk\omega_{\text{sw}}} \cdot \overrightarrow{V_{b1,k}}. \tag{15}$$

By equating R.H.S. of (14) and (15), the value of $L_{eq:1}$ is obtained as follows:

$$L_{eq:1} = \frac{1}{[\mathbf{L^{-1}}]_{(1,1)}}. \tag{16}$$

With the value obtained for equivalent series inductance $L_{eq:1}$ in (16), the next step is to compute the value of $V_{eq:1,k}$ by setting $\overrightarrow{V_{b1,k}}$ to zero. In this scenario, the port 1 current, $\overrightarrow{I_{b1,k}}$, can be written in two ways: 1) from Fig. 3(b) as given in (17); and 2)

by using (7) and (13) as given as follows:

$$\overrightarrow{I_{b1,k}} = -\frac{\overrightarrow{V_{eq:1,k}}}{jk\omega_{\text{sw}}L_{eq:1}} \tag{17}$$

$$\overrightarrow{I_{b1,k}} = \frac{1}{jk\omega_{\text{sw}}} \cdot \text{row}_1(\mathbf{L^{-1}}) \cdot \begin{bmatrix} 0 \\ V_{b2,k} \\ V_{b3,k} \\ V_{b4,k} \end{bmatrix}. \tag{18}$$

By equating R.H.S. of (17) and (18), the expression for the the equivalent reflected voltage from all the other ports on port 1 ($\overrightarrow{V_{eq:1,k}}$) is obtained as follows:

$$\overrightarrow{V_{eq:1,k}} = -L_{eq:1} \cdot \text{row}_1(\mathbf{L^{-1}}) \cdot \begin{bmatrix} 0 \\ V_{b2,k} \\ V_{b3,k} \\ V_{b4,k} \end{bmatrix}. \tag{19}$$

D. General Solution for jth Port of n-Port MAB

The above solution can be generalized for jth port of an n-port MAB to find $L_{eq:j}$ and $\overrightarrow{V_{eq:j,k}}$ as shown as follows:

$$L_{eq:j} = \frac{1}{[\mathbf{L^{-1}}]_{(j,j)}} \tag{20}$$

$$\overrightarrow{V_{eq:j,k}} = -\sum_{\substack{m=1 \\ m\neq j}}^{n} \frac{[\mathbf{L^{-1}}]_{(j,m)}}{[\mathbf{L^{-1}}]_{(j,j)}} \cdot \overrightarrow{V_{bm,k}}. \tag{21}$$

It should be noted that, $\overrightarrow{V_{eq:j,k}}$ corresponds to the kth harmonic of the $V_{eq:j}$. To obtain the time domain reconstruction of $V_{eq:j}$, harmonic superposition is used as shown in (22).

$$v_{eq:j}(t) = \sum_{\substack{m=0 \\ k=2m+1}}^{H_{\max}} \left|\overrightarrow{V_{eq:j,k}}\right| \sin\left(k\omega_{\text{sw}}t + \angle\overrightarrow{V_{eq:j,k}}\right). \tag{22}$$

To summarize, the $L_{eq:j}$ of the jth port can be obtained by the (j,j)th element of the $\mathbf{L^{-1}}$ matrix and $V_{eq:j,k}$ can be obtained from the jth row element of $\mathbf{L^{-1}}$ by using (21). Hence, just by taking the inverse of $\mathbf{L}$ matrix once, the $L_{eq:j}$ and the scaling factor to the branch voltages to obtain $V_{eq:j,k}$ of all the ports can be obtained. It is worth mentioning that the proposed impedance matrix-based frequency domain modeling approach provides a convenient method to analyze the MAB converter operation, especially in terms of simplifying the ZVS analysis. The proposed framework uses a simple set of matrix operations where the solution is directly extendable for an n-port MAB converter, while capturing all magnetic coupling relationships through the full-order inductance matrix.

E. ZVS Criterion for MAB Full-Bridge Port

With the values obtained for $L_{eq:j}$ and $v_{eq:j}(t)$, each MAB port can be analyzed for ZVS criterion as a DAB converter. Extending from the results obtained for DAB converter in [25], a comprehensive analysis of the ZVS transition is presented hereinafter for the jth port of the MAB converter to find the necessary and sufficient conditions. The switching transitions of the full-bridge port is divided into two categories: 1) when v_{bj} is a square-wave ($\delta_j = 0$); 2) when v_{bj} is a quasi-square wave ($\delta_j \neq 0$). Table I tabulates the conditions for complete ZVS transition of each switch in port j. Here, $E_{L_{eq:j}} = \frac{1}{2}L_{eq:j}i_{bj}^2(t_0)$, where t_0 is the switching instance. $Q_{oss}(V_j) = \int_0^{V_j} C_{oss}(v)dv$ refers to the total charge in switch output capacitance when blocking a voltage of V_j, and $C_{oss}(v)$ is the voltage dependent nonlinear output capacitance of the switch. $v_{eq:j}(t_0)$ is the equivalent voltage from other ports obtained using (22). Fig. 4(a) illustrates the charge flow for ZVS turn-ON scenario for $S_{j:1}$ and $S_{j:4}$. At the beginning of the transition, $S_{j:2}$ and $S_{j:3}$ are turned OFF. Since $i_{bj}(t_0) < 0$, the output capacitance of $S_{j:1}$ and $S_{j:4}$ are discharged while output capacitance of $S_{j:2}$ and $S_{j:3}$ are charged. The total charge that needs to be displaced is $2Q_{oss}(V_j)$, which flows out of $v_{eq:j}(t_0)$. Therefore, the energy required for this process is $-2Q_{oss}(V_j) \cdot v_{eq:j}(t_0)$. It should be noted that the source V_j does not consume any net energy in this transition. The Fig. 4(b) illustrates the example charge flow for ZVS turn-ON scenario for $S_{j:1}$ with $\delta_j \neq 0$. Assuming $S_{j:1}$ and $S_{j:2}$ to be the leading leg, $S_{j:3}$ is ON and $S_{j:4}$ is OFF. At the beginning of the transition $S_{j:2}$ turns OFF. Assuming $i_{bj}(t_0) < 0$ a net charge of $2Q_{oss}(V_j)$ flows out of $v_{eq:j}(t_0)$, charging the output capacitance of $S_{j:2}$ to V_j and discharging the output capacitance of $S_{j:1}$ to 0V. Furthermore, during the process of charging $S_{j:2}$, a net charge of $Q_{oss}(V_j)$ flows out of V_j to supply energy. Hence, the total energy required for this transition is $Q_{oss}(V_j) \cdot (-2v_{eq:j}(t_0) - V_j)$. Similar analysis can be conducted for all the transitions to obtain the minimum energy conditions in Table I.

TABLE I
NECESSARY AND SUFFICIENT CONDITIONS FOR ZVS TURN-ON

δ	Necessary condition	Switch	$(E_{L_{eq:j}})_{\min}$
$\delta_j = 0$	$i_{bj}(t_0) < 0$	$S_{j:1}$ and $S_{j:4}$	$-2Q_{oss}(V_j) \cdot v_{eq:j}(t_0)$
	$i_{bj}(t_0) > 0$	$S_{j:2}$ and $S_{j:3}$	$+2Q_{oss}(V_j) \cdot v_{eq:j}(t_0)$
$\delta_j \neq 0$	$i_{bj}(t_0) < 0$	$S_{j:1}$	$Q_{oss}(V_j) \cdot (-2v_{eq:j}(t_0) - V_j)$
	$i_{bj}(t_0) > 0$	$S_{j:2}$	$Q_{oss}(V_j) \cdot (+2v_{eq:j}(t_0) - V_j)$
	$i_{bj}(t_0) > 0$	$S_{j:3}$	$Q_{oss}(V_j) \cdot (+2v_{eq:j}(t_0) + V_j)$
	$i_{bj}(t_0) < 0$	$S_{j:4}$	$Q_{oss}(V_j) \cdot (-2v_{eq:j}(t_0) + V_j)$

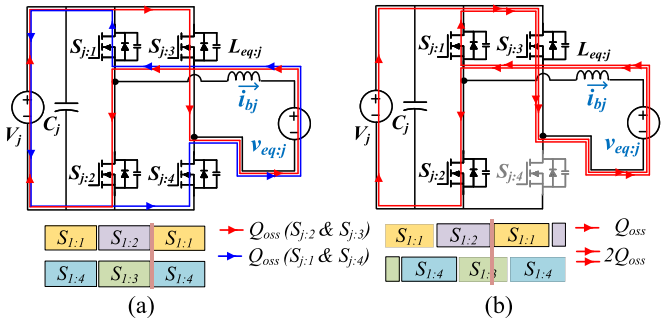

Fig. 4. Illustration of charge flow during ZVS transition using proposed DAB equivalent representation of MAB converter jth port. (a) Turn-ON transition of $S_{j:1}$ & $S_{j:4}$. (b) Turn-ON transition of $S_{j:1}$.

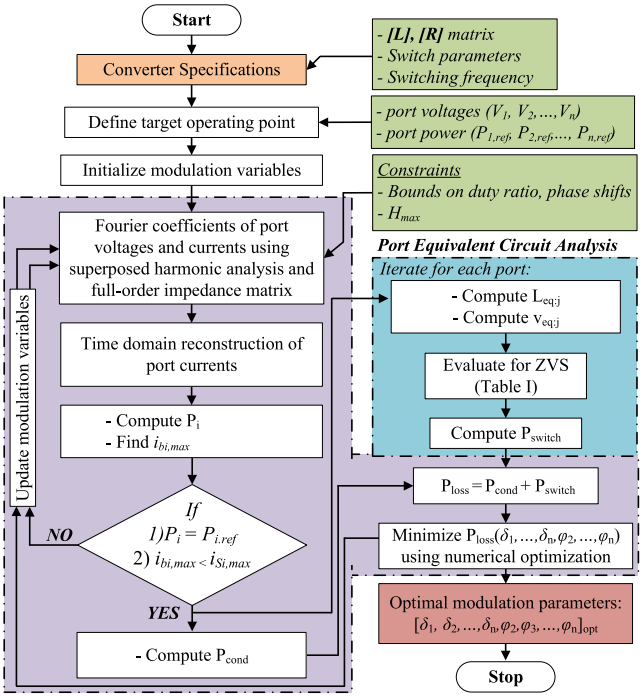

Fig. 5. Flowchart illustrating the key steps involved in obtaining optimal modulation parameters.

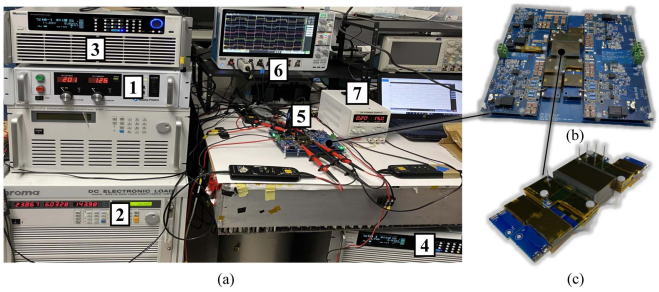

Fig. 6. (a) Experimental setup: 1) Port 1 DC Power Supply. 2) Port 2 DC electronic load. 3) Port 3 DC electronic load. 4) Port 4 DC electronic load. 5) MAB hardware prototype. 6) Oscilloscope. 7) Auxiliary power supply. (b) Four-port MAB converter. (c) Four-port planar magnetics with branch inductors.

III. Algorithm to Find Optimal Modulation Parameters

In this section, a systematic algorithm for obtaining the modulation parameters ($\delta_{\rm i}$ and $\varphi_{\rm i}$) of the MAB converter is presented. The algorithm is executed using the results obtained in Section II and with the purpose of achieving the optimal converter operation with minimal losses.

The optimization variables are $\delta_{\rm i}$ and $\varphi_{\rm i}$ for $i = 1, 2, \ldots, n$ whereas the fixed variables are the port dc voltages, V_i. There are three parts which formulate the nonlinear constrained optimization problem which are as follows: 1) Equality constraints: Where the resultant boundary conditions should be equal to the reference boundary conditions; 2) inequality constraints: Where the resultant boundary conditions should be greater than (or less than) the reference boundary conditions, and 3) objective

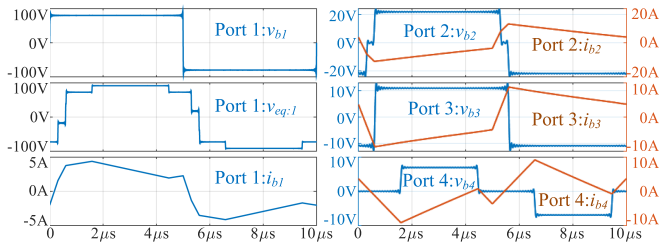

Fig. 7. Equivalent circuit waveforms for operating point: $[V_1, V_2, V_3, V_4, P_{\rm out}]$; [160 V, 22 V, 11 V, 7 V, 225 W].

function: A function which comprises of the major optimization targets that should be minimized (or maximized). Within the context of the optimal modulation of the MAB converter for a given operating point, the equality constraints are the resultant port powers (9), which must equal the referenced powers ($P_{i,\rm ref}$) as shown in (23).

$$P_i = P_{i,\rm ref} \text{ for } i = 1, 2, \ldots, n. \tag{23}$$

The safe operation of the proposed converter is attained by ensuring that the instantaneous inductor branch currents never exceed the maximum switch current ratings over the switching cycle. Hence, the inequality boundary conditions are set as the maximum instantaneous branch currents ($i_{bi,\rm max}$), which should always be less than the maximum switch current ($i_{S_i,\rm max}$) in the corresponding ports, as given in (24).

$$i_{bi,\rm max} < i_{S_i,\rm max} \text{ for } i = 1, 2, \ldots, n. \tag{24}$$

The objective function of this nonlinear optimization algorithm is to minimize the total losses ($P_{\rm loss}$) present during the converter operation which in turn maximizes its efficiency. The two major loss mechanisms that are considered in the optimization process are the conduction loss ($P_{\rm cond}$) and switching loss ($P_{\rm switch}$). The overall constrained optimization problem is summarized in (25).

$$\begin{aligned} \min_{[\delta_1,\ldots,\delta_{\rm n},\varphi_2,\ldots,\varphi_{\rm n}]} \quad & P_{\rm loss}(= P_{\rm loss} + P_{\rm switch}) \\ \delta_{\rm i}\sim[0,\pi/2];\varphi_{\rm i}\sim[-\pi/2,\pi/2] & \\ \text{s.t.} \quad & P_i = P_{i,\rm ref} \\ & i_{bi,\rm max} < i_{S_i,\rm max}. \end{aligned} \tag{25}$$

In this article, the conduction loss is calculated using (12). Whereas, to determine the switching losses, the turn-ON switching transitions are initially categorized as either a full-ZVS or a hard-switching transition. It should be noted that the turn-OFF losses are considered to be negligible for this case study due to the use of GaN switches in the hardware prototype. This switching transition categorization is performed using the energy conditions and the current direction requirements shown in Table I. In this analysis, a dead-time of 60 ns is considered. In this study, a ZVS transition is considered to have no switching losses present resulting from the use of GaN switches in the hardware. Whereas, in the event of a hard-switching transition, the switching losses are computed using the method in [26]. However, when Si or SiC switches which have nonnegligible turn-OFF

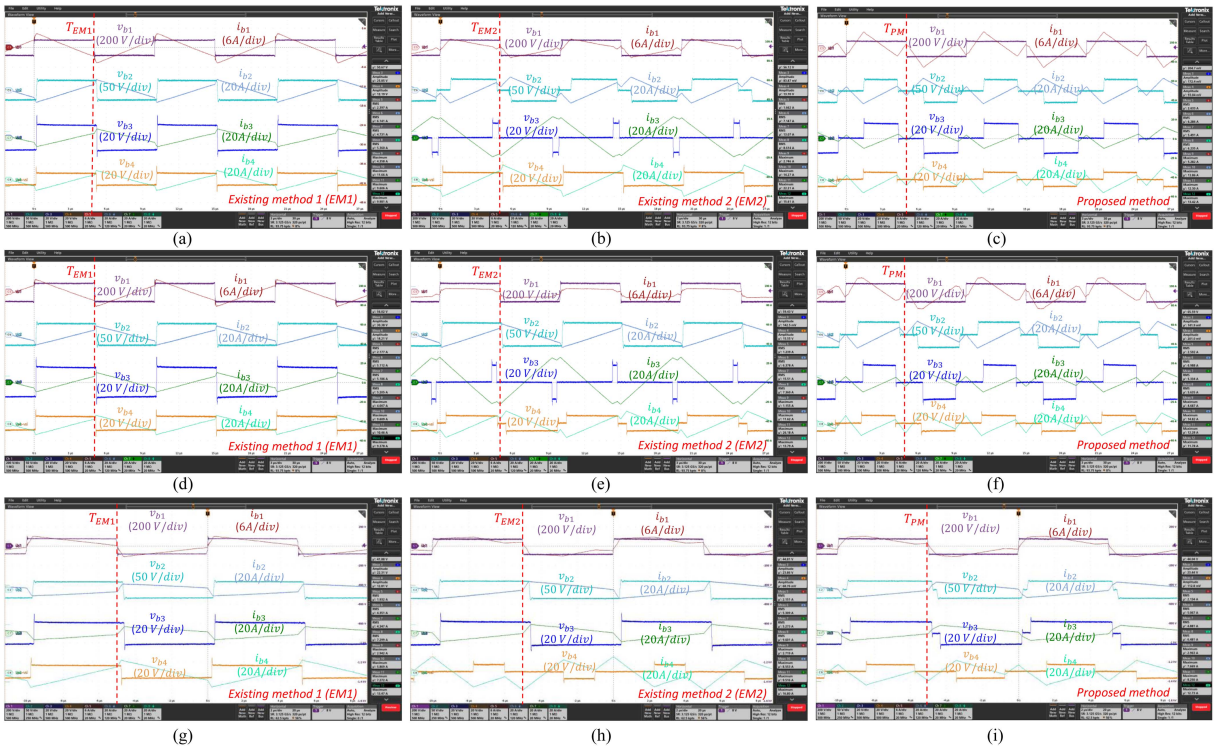

Fig. 8. Experimental waveforms of branch voltages and branch currents for EM1, EM2 and proposed method at $\{[V_1, V_2, V_3, V_4], [P_2{:}P_3{:}P_4]\}$ = (a) $\{[160\text{V}, 28\text{V}, 14\text{V}, 7\text{V}], [0.6 : 0.25 : 0.15]\}$, (b) $\{[190\text{ V}, 30\text{ V}, 16\text{ V}, 8\text{ V}], [0.6 : 0.25 : 0.15]\}$, (c) $\{[160\text{ V}, 22\text{ V}, 11\text{ V}, 7\text{ V}], [0.6 : 0.25 : 0.15]\}$, (d) $\{[160\text{ V}, 30\text{ V}, 16\text{ V}, 8\text{ V}], [0.6 : 0.25 : 0.15]\}$.

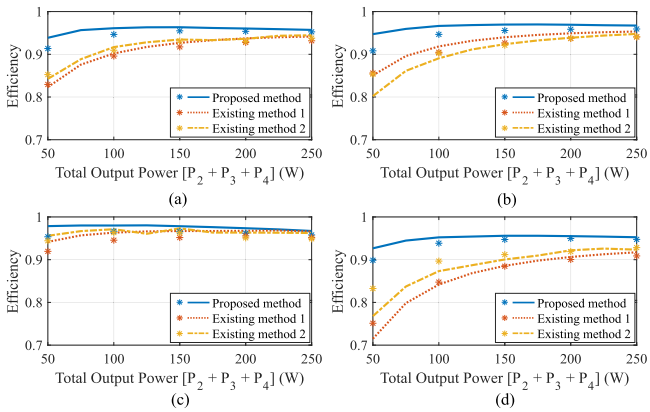

Fig. 9. Efficiency comparison between the existing and proposed modulation approach; "*" represents the experimental efficiency measurements, $\{[V_1, V_2, V_3, V_4], [P_2{:}P_3{:}P_4]\}$ = (a) $\{[160\text{ V}, 28\text{ V}, 14\text{ V}, 7\text{ V}], [0.6 : 0.25 : 0.15]\}$, (b) $\{[190\text{ V}, 30\text{ V}, 16\text{ V}, 8\text{ V}], [0.6 : 0.25 : 0.15]\}$, (c) $\{[160\text{ V}, 22\text{ V}, 11\text{ V}, 7\text{ V}], [0.6 : 0.25 : 0.15]\}$, (d) $\{[160\text{ V}, 30\text{ V}, 16\text{ V}, 8\text{ V}], [0.6 : 0.25 : 0.15]\}$.

losses are used, the losses incurred in the ZVS turn-ON transition can be modeled using the method demonstrated in [29]. Due to the highly nonlinear nature of the MAB modulation variables and circuit parameters present in the optimization algorithm, a gradient-based numerical optimization routine utilizing the MATLAB Optimization Tool Box "fmincon" is implemented in this approach. As an alternative, to avoid potential local-minima related issues in gradient-based methods, other heuristic/global search optimization routines can be used. Evaluating the trade-off between the execution time and the desired optimization accuracy is a factor when selecting the preferred optimization tool. The major steps in the proposed constrained nonlinear optimization algorithm for obtaining the optimal modulation parameters are summarized in the flowchart shown in Fig. 5.

TABLE II
AVERAGE COMPUTATION TIME COMPARISON

Method	Existing method 1	Existing method 2	Proposed method
Average time (s)	3.59	15.12	17.68

In order to compare the computational burden of the existing and proposed method, the averaged execution times are measured on MATLAB R2021b running on a computer with Intel Core i3-10100 CPU and 16 GB of RAM. The results are provided in Table II for the four-port MAB converter discussed in Section IV.

IV. RESULTS AND DISCUSSION

A four-port MAB converter design is used to validate the proposed modeling and optimal modulation scheme. The key specifications of the MAB converter are tabulated in Table III. In terms of the ac link, a planar transformer with external branch indicators is used. A photograph of the magnetic structure is shown in Fig. 6(c). To obtain the inductance and resistance

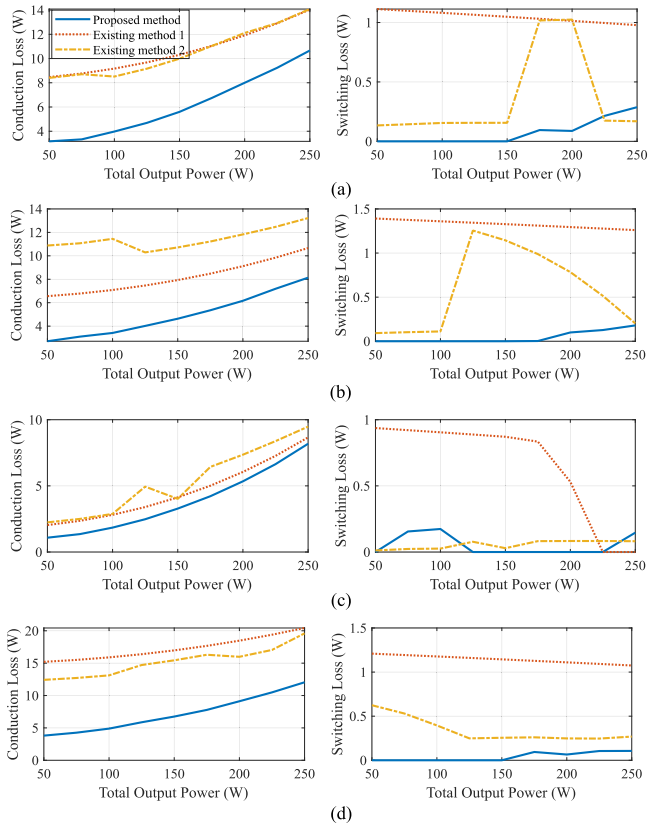

Fig. 10. Loss breakdown comparison between the existing and proposed modulation approach, $\{[V_1,\ V_2,\ V_3,\ V_4],\ [P_2{:}P_3{:}P_4]\}$ = (a) {[160 V, 28 V, 14 V, 7 V], [0.6 : 0.25 : 0.15]}, (b) {[190 V, 30 V, 16 V, 8 V], [0.6 : 0.25 : 0.15]}, (c) {[160 V, 22 V, 11 V, 7 V], [0.6 : 0.25 : 0.15]}, (d) {[160 V, 30 V, 16 V, 8 V], [0.6 : 0.25 : 0.15]}.

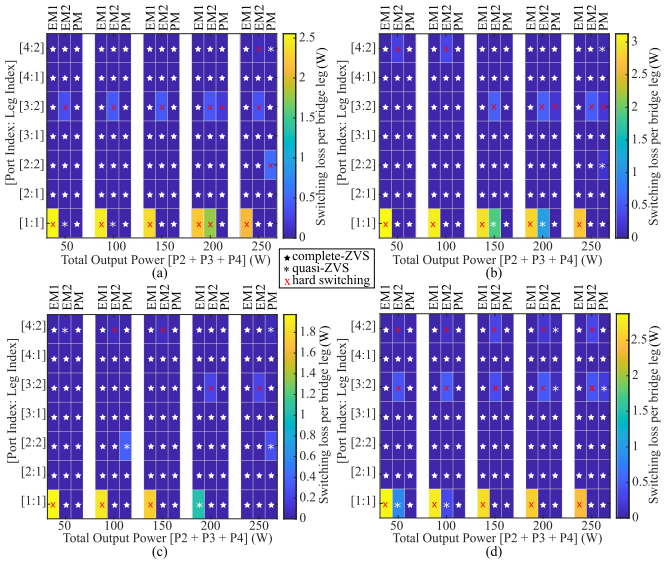

Fig. 11. ZVS performance comparison between the existing and proposed modulation (PM) approaches, $\{[V_1,\ V_2,\ V_3,\ V_4],\ [P_2{:}P_3{:}P_4]\}$ = (a) {[160V, 28 V, 14 V, 7 V], [0.6 : 0.25 : 0.15]}, (b) {[190 V, 30 V, 16 V, 8 V], [0.6 : 0.25 : 0.15]}, (c) {[160 V, 22 V, 11 V, 7 V], [0.6 : 0.25 : 0.15]}, (d) {[160 V, 30 V, 16 V, 8 V], [0.6 : 0.25 : 0.15]}.

TABLE III
FOUR-PORT MAB CONVERTER SPECIFICATIONS

Parameter	Port 1	Port 2	Port 3	Port 4
Bridge configuration	Half-bridge	Full-bridge	Full-bridge	Full-bridge
Port voltage	160 – 200 V	20 – 30 V	8 – 16 V	4 – 8 V
Max power	250 W	150 W	62.5 W	37.5 W
Switching frequency (f_{sw})		100kHz		
Physical TX turns	16	4	2	1
Branch inductance	N/A	1.34 μH	1.04 μH	0.275 μH
MOSFET	GS66506T	EPC2022	EPC2020	EPC2023
Gate-driver	Si8271AB	LMG1205	LMG1205	LMG1205
Signal isolator	Gate-Driver	Si8620	Si8620	Si8620

matrix of the magnetic design, a comprehensive eddy current FEA simulation sweep is conducted for the entire structure using ANSYS Maxwell. The $\mathbf{L}$ and $\mathbf{R}$ corresponding to 100 kHz are shown in (26) and (27). The obtained modulation parameters are realized in Texas Instruments' TMS320F28377D DSP using curve-fit equations and is provided as feed-forward, as presented in [17]. A constant dead-time of 60 ns is provided between the complementary switching pulses.

$$\mathbf{L}(mH) = \begin{bmatrix} 3.9204 & 0.9800 & 0.4901 & 0.2450 \\ 0.9800 & 0.2463 & 0.1225 & 0.0612 \\ 0.4901 & 0.1225 & 0.0623 & 0.0306 \\ 0.2450 & 0.0612 & 0.0306 & 0.0156 \end{bmatrix} \tag{26}$$

$$\mathbf{R}(m\Omega) = \begin{bmatrix} 166.64 & 22.09 & 11.92 & 5.42 \\ 22.09 & 18.99 & 2.59 & 1.22 \\ 11.93 & 2.59 & 11.62 & 0.80 \\ 5.43 & 1.23 & 0.801 & 3.72 \end{bmatrix}. \tag{27}$$

By using the FEA-extracted high frequency link information, the port equivalent DAB configuration is created for each port to investigate the ZVS transitions. By using (20), the obtained port equivalent inductances are shown in (28). Furthermore, the FEA obtained $\mathbf{L}$ matrix information is used to simplify (21) as given in (29). It should be noted that with the proposed approach, $v_{eq:j}(t)$ for each port is obtained by the summation of each branch voltage multiplied by a scalar term, which itself is independent of the modulation variables and harmonic number. This makes the entire ZVS evaluation process computationally efficient and substantially improves the scalability of the proposed method to MAB converter with large number of ports. As an example, the Fig. 7 illustrates the reconstructed time-domain waveforms for the port 1 equivalent circuit. $v_{eq:1}(t)$ represents the resultant equivalent voltage by combing the effects from all other ports coupled through the magnetic link. The instantaneous voltages and currents at the switching transitions are used to analyze the port 1 in terms of ZVS.

$$\mathbf{L}_{eq}(\mu H) = \begin{bmatrix} 13.09 & 1.315 & 1.048 & 0.299 \end{bmatrix} \tag{28}$$

$$\begin{bmatrix} v_{eq:1}(t) \\ v_{eq:2}(t) \\ v_{eq:3}(t) \\ v_{eq:4}(t) \end{bmatrix} = \begin{bmatrix} 0.000 & 2.515 & 1.592 & 2.705 \\ 0.253 & 0.000 & -0.019 & -0.003 \\ 0.127 & -0.015 & 0.000 & 0.022 \\ 0.062 & -0.0007 & 0.0062 & 0.000 \end{bmatrix} \begin{bmatrix} v_{b1}(t) \\ v_{b2}(t) \\ v_{b3}(t) \\ v_{b4}(t) \end{bmatrix}. \tag{29}$$

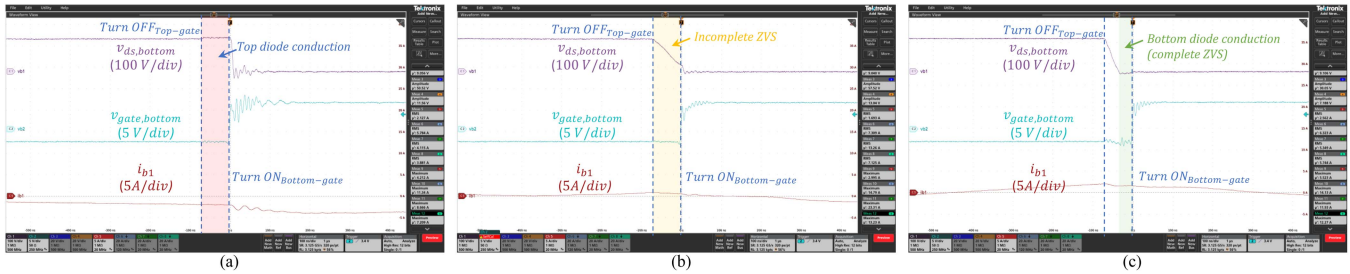

Fig. 12. Switching transition of port 1 bottom switch for: (a) EM1 at T_{EM1} in Fig. 8(a), (b) EM2 at T_{EM2} in Fig. 8(b), and (c) proposed method at T_{PM} in Fig. 8(c).

To compare the performance of the proposed framework against existing methods, Fig. 8 shows the experimental results for branch voltages and currents of the MAB converter for various port voltages and power levels. Fig. 8(a), (d), and (g) shows the experimental result for conventional control of MAB converters with only phase shift control (referred to as existing method 1, EM1) [13], [14], [15]. The modulation of the converter with both phase shift and duty ratio control is shown in Fig. 8(b), (e), and (h) and this method is referred to as existing method 2 (EM2) [17]. In the above two methods (EM1 and EM2), star-model of the magnetic link, which is a reduced order model is used. Fig. 8(c), (f), and (i) shows the experimental result using the proposed method incorporating phase shift, duty ratio, and the full order impedance matrix of the high frequency ac link. It should be noted that, since there are different combinations of modulation variables to obtain the same power flow, the profile of branch voltages and currents are different in all three methods.

The branch voltages in EM1 are square waveforms, due to the absence of duty ratio control. In contrast, the branch voltages in EM2 and the proposed method can be either a square waveform or a quasi-square waveform. With increased flexibility in modulation and better representation of the magnetic coupling, the proposed method finds the optimal modulation parameters to reduce the losses in the system. This is validated by the comparison of efficiencies of all the three methods and the observation of switching transitions, explained hereinafter.

The efficiency of the MAB converter obtained by using the proposed method is compared with the existing methods in Fig. 9, where the experimental measurements are denoted by "*". Along with the usage of duty-ratio control (which provide more degrees of freedom) the increased knowledge of the magnetic coupling and improved estimation of conduction loss using $\mathbf{R}$ matrix enables the proposed method to have superior efficiency compared to EM1 and EM2. The slight discrepancy in the experimental efficiency could be attributed to the variation in the ON-state resistance of the switches and ESR losses in the capacitors.

The converter loss breakdown corresponding to the same set of operating points (shown in Fig. 9) are illustrated in Fig. 10. In terms of switching losses, the EM1 does not use the switching losses in the objective function as it does not model soft-switching behavior in the MAB converter. Therefore, EM1 primarily uses conduction loss minimization to improve the converter efficiency without having any control over the switching loss. This could potentially lead to high switching losses in the converter negating the benefits achieved from conduction loss minimization. In EM2, the ZVS conditions are identified using the star-model of the MAB converter's magnetic link with the corresponding port referred inductance value. Subsequently, the non-ZVS (hard switching) switching transitions are used to create a proxy for the switching losses. Since both conduction and switching losses are based on proxy variables in EM2, the relative magnitude information is not accurately captured when creating the objective function for the total losses in the converter, leading to inaccurate representation of total losses in the converter. Furthermore, the star-model of the magnetic link is not a full-order model, which leads to inaccuracies in terms of analyzing the energy condition to achieve ZVS. In contrast, the proposed method uses the full order inductance matrix to derive the expressions for ZVS conditions, and for the non-ZVS operating points the switching losses are estimated accurately considering the both the direction and magnitude condition (energy condition) of branch currents as shown in Table I.

The comparison of switching behavior in the MAB converter using existing (EM1 and EM2) and proposed method for the same set of operating points are shown in Fig. 11. The high switching losses observed in EM1 in Fig. 10 can be explained by observing Fig. 11 where it is evident that the half-bridge leg 1 of the port 1 incurs a hard switching transitions leading to increased switching losses. Since port 1 processes the highest amount of power/voltage, achieving ZVS in port 1 is critical to minimize the switching losses in the converter. In contrast, the proposed method achieves complete-ZVS for all the switching transitions in the port 1 minimizing the switching losses in the converter across all operating points. As the objective in the proposed method is to minimize the total losses in the converter, the proposed method achieves complete-ZVS in all switching legs especially in light-load conditions where the converter conduction losses are low and comparable to the switching losses.

Furthermore, the proposed methodology to determine and utilize $L_{eq:j}$ and $v_{eq:j}$ (where $j = 1, 2, 3,$ or 4) results in modulation parameters that ensure full soft switching. This is validated from the switching transitions of each port for the three methods. As an example, Fig. 12 are expanded versions of time instances T_{EM1}, T_{EM2}, and T_{PM} of Fig. 8, with the drain-source voltage of bottom switch in port 1 leg, corresponding gate-source voltage

and branch current of port 1. It can be seen that the modulating parameters obtained using EM1 results in hard turn ON, while EM2 leads to incomplete ZVS and the proposed method leads to complete ZVS transition, resulting in lowest losses. The above experimental results show the efficacy of the proposed method over the existing methods when implemented on the same hardware prototype.

V. Conclusion

A comprehensive approach to model and obtain optimal modulation parameters for an n-port MAB converter is presented in this article. The proposed model utilizes the full-order impedance matrix of the high frequency ac link to capture all magnetic coupling relationships, as well as resistive characteristics which affect the power flow, ZVS criteria, and the losses in the converter. An analytical method is devised to determine the equivalent inductance and equivalent reflected voltage from each port using the inductance matrix. These values are further used in the port equivalent representation of the MAB converter which enables accurate evaluation of ZVS criteria for all the switching transitions. Furthermore, the resistance matrix along with the branch currents are used to accurately capture the conduction losses incurred in the system. With the proposed methods for finding the switching and conduction losses with the frequency domain modeling of the converter, an algorithm is proposed to find the optimal modulation parameters. The proposed scheme is then validated experimentally using a four-port GaN-based MAB converter hardware prototype. It is validated that using a full order impedance matrix modeling, which captures the complex coupling and loss mechanisms, the proposed optimal modulation method enhances the efficiency of the system. In addition to improved operation of existing designs (higher efficiency and ZVS), the proposed modeling and optimization approach also provides a generalized platform for design space optimizations of MAB converters, which can be used optimally design switches and magnetics for MAB converters. With accurate estimation of voltages and currents in the system, the framework also allows for addition of other loss mechanisms to expand the optimization objective functions and constraints.

Acknowledgment

The authors would like to thank Dr. Apurv Kumar Yadav and Dr. Jianfei Chen for their valuable feedback.

References

[1] D. Jiang et al., "Multiobjective optimization considering PET's vibration suppression of dual active bridge converter based on BP-NSGA-II," *IEEE Trans. Power Electron.*, vol. 39, no. 2, pp. 2226–2236, Feb. 2024.

[2] Y. Cao, K. Ngo, and D. Dong, "A scalable electronic-embedded transformer, a new concept toward ultra-high-frequency high-power transformer in DC–DC converters," *IEEE Trans. Power Electron.*, vol. 38, no. 8, pp. 9278–9293, Aug. 2023.

[3] D. Costinett, D. Maksimovic, and R. Zane, "Design and control for high efficiency in high step-down dual active bridge converters operating at high switching frequency," *IEEE Trans. Power Electron.*, vol. 28, no. 8, pp. 3931–3940, Aug. 2013.

[4] Y. Chen, P. Wang, Y. Elasser, and M. Chen, "Multicell reconfigurable multi-input multi-output energy router architecture," *IEEE Trans. Power Electron.*, vol. 35, no. 12, pp. 13210–13224, Dec. 2020.

[5] S. Falcones, R. Ayyanar, and X. Mao, "A DC–DC multiport-converter-based solid-state transformer integrating distributed generation and storage," *IEEE Trans. Power Electron.*, vol. 28, no. 5, pp. 2192–2203, May 2013.

[6] L. F. Costa, G. Buticchi, and M. Liserre, "Optimum design of a multiple-active-bridge DC–DC converter for smart transformer," *IEEE Trans. Power Electron.*, vol. 33, no. 12, pp. 10112–10121, Dec. 2018.

[7] S. Zou, J. Lu, and A. Khaligh, "Modelling and control of a triple-active-bridge converter," *IET Power Electron.*, vol. 13, no. 5, pp. 961–969, 2020. [Online]. Available: https://ietresearch.onlinelibrary.wiley.com/doi/abs/10.1049/iet-pel.2019.0920

[8] M. Liu, Y. Chen, Y. Elasser, and M. Chen, "Dual frequency hierarchical modular multilayer battery balancer architecture," *IEEE Trans. Power Electron.*, vol. 36, no. 3, pp. 3099–3110, Mar. 2021.

[9] G. Buticchi, L. F. Costa, D. Barater, M. Liserre, and E. D. Amarillo, "A quadruple active bridge converter for the storage integration on the more electric aircraft," *IEEE Trans. Power Electron.*, vol. 33, no. 9, pp. 8174–8186, Sep. 2018.

[10] C. Gu, Z. Zheng, L. Xu, K. Wang, and Y. Li, "Modeling and control of a multiport power electronic transformer (PET) for electric traction applications," *IEEE Trans. Power Electron.*, vol. 31, no. 2, pp. 915–927, Feb. 2016.

[11] D. Xie, C. Lin, H. Lin, W. Liu, Y. Du, and T. Basler, "OC switch fault diagnosis, pre- and postfault DC voltage balancing control for a CHBMC using SVM concept," *IEEE Trans. Power Electron.*, vol. 39, no. 1, pp. 677–692, Jan. 2024.

[12] B. Liu, W. Song, Y. Li, and B. Zhan, "Performance improvement of DC capacitor voltage balancing control for cascaded H-bridge multilevel converters," *IEEE Trans. Power Electron.*, vol. 36, no. 3, pp. 3354–3366, Mar. 2021.

[13] Y. Chen, P. Wang, H. Li, and M. Chen, "Power flow control in multi-active-bridge converters: Theories and applications," in *Proc. 2019 IEEE Appl. Power Electron. Conf. Expo.*, Mar. 2019, pp. 1500–1507.

[14] P. Wang, Y. Chen, J. Yuan, R. C. N. Pilawa-Podgurski, and M. Chen, "Differential power processing for ultra-efficient data storage," *IEEE Trans. Power Electron.*, vol. 36, no. 4, pp. 4269–4286, Apr. 2021.

[15] O. M. Hebala, A. A. Aboushady, K. H. Ahmed, and I. Abdelsalam, "Generalized active power flow controller for multiactive bridge DC–DC converters with minimum-current-point-tracking algorithm," *IEEE Trans. Ind. Electron.*, vol. 69, no. 4, pp. 3764–3775, Apr. 2022.

[16] B. Majmunović et al., "1 kV, 10-kW SiC-Based quadruple active bridge DCX stage in a DC to three-phase AC module for medium-voltage grid integration," *IEEE Trans. Power Electron.*, vol. 37, no. 12, pp. 14631–14646, Dec. 2022.

[17] S. Dey and A. Mallik, "Switching network loss minimization through multivariable modulation in a multiactive bridge converter," *IEEE Trans. Ind. Electron.*, vol. 70, no. 11, pp. 10833–10847, Nov. 2023.

[18] M. Chen and C. R. Sullivan, "Unified models for coupled inductors applied to multiphase PWM converters," *IEEE Trans. Power Electron.*, vol. 36, no. 12, pp. 14155–14174, Dec. 2021.

[19] S. Zou, C. Singhabahu, J. Chen, and A. Khaligh, "A comprehensive design approach for a three-winding planar transformer," *IET Power Electron.*, vol. 15, no. 8, pp. 717–727, 2022. [Online]. Available: https://onlinelibrary.wiley.com/doi/abs/10.1049/pel2.12261

[20] R. Erickson and D. Maksimovic, "A multiple-winding magnetics model having directly measurable parameters," in *Proc. PESC 98 Record. 29th Annu. IEEE Power Electron. Specialists Conf.*, May 1998, vol. 2, pp. 1472–1478.

[21] C. Singhabahu, A. Singh, A. Hasnain, A. K. Yadav, J. Chen, and A. Khaligh, "Design and optimization of planar magnetics for a quadruple-active-bridge converter," in *Proc. 2022 IEEE Ind. Appl. Soc. Annu. Meeting*, Oct. 2022, pp. 1–8.

[22] J. Spreen, "Electrical terminal representation of conductor loss in transformers," *IEEE Trans. Power Electron.*, vol. 5, no. 4, pp. 424–429, Oct. 1990.

[23] A. K. Jain and R. Ayyanar, "PWM control of dual active bridge: Comprehensive analysis and experimental verification," *IEEE Trans. Power Electron.*, vol. 26, no. 4, pp. 1215–1227, Apr. 2011.

[24] D. Mou et al., "Reactive power minimization for modular multi-active-bridge converter with whole operating range," *IEEE Trans. Power Electron.*, vol. 38, no. 7, pp. 8011–8015, Jul. 2023.

[25] Y. Yan, H. Gui, and H. Bai, "Complete ZVS analysis in dual active bridge," *IEEE Trans. Power Electron.*, vol. 36, no. 2, pp. 1247–1252, Feb. 2021.

[26] M. Kasper, R. M. Burkart, G. Deboy, and J. W. Kolar, "ZVS of power MOSFETs revisited," *IEEE Trans. Power Electron.*, vol. 31, no. 12, pp. 8063–8067, Dec. 2016.

[27] H. Wang, Y. Zeng, S. Ji, Z. Zhao, L. Yuan, and X. Mo, "ZVS soft switching operation region analysis of modular multi active bridge converter under single phase shift control," *IEEE Trans. Ind. Electron.*, vol. 70, no. 7, pp. 6865–6875, Jul. 2023.
[28] S. S. Shah, V. M. Iyer, and S. Bhattacharya, "Exact solution of ZVS boundaries and AC-Port currents in dual active bridge type DC–DC converters," *IEEE Trans. Power Electron.*, vol. 34, no. 6, pp. 5043–5047, Jun. 2019.
[29] D. Christen and J. Biela, "Analytical switching loss modeling based on datasheet parameters for MOSFETs in a half-bridge," *IEEE Trans. Power Electron.*, vol. 34, no. 4, pp. 3700–3710, Apr. 2019.

Chanaka Singhabahu (Member, IEEE) received the Bachelor of Science degree in electronic and telecommunication engineering from the University of Moratuwa, Moratuwa, Sri Lanka, in 2017, and the M.S. and Ph.D. degrees in electrical engineering from the University of Maryland (UMD) College Park, MD, USA, in 2023.

He is currently a Sr. Power Electronics Engineer with Rivian Automotive, Inc., Irvine, CA, USA. His research interests include design, modeling, control and development of highly efficient, reliable, and power-dense wide-bandgap device-based power electronic converters for transportation electrification and renewable energy systems.

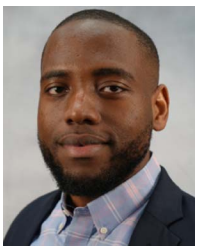

Ayooluwa Ajiboye (Student Member, IEEE) received the B.S. degree in electrical and electronics engineering from Covenant University, Ogun State, Nigeria, in 2019. He is currently working toward the M.S. and Ph.D. degrees in electrical and computer engineering with the University of Maryland, College Park, MD, USA.

His current research interests include the modeling, design, optimization and control of bidirectional high-frequency dc–ac converters for applications in renewable energy and transportation electrification, SiC bare-die based traction inverters, solar microinverters, grid-connected inverters, battery management systems, characterization of wide-bandgap power switches, and the characterization of the effects of parasitics present in the commutation power loop of dc-link based power converters.

Rakesh Resalayyan (Member, IEEE) received the B.Tech. degree in electrical and electronics engineering from the College of Engineering, Trivandrum, India, in 2014, and the M.Tech. and Ph.D. degrees in power electronics from the Department of Electronic Systems Engineering, Indian Institute of Science (IISc), Bengaluru, India, in 2017 and 2021, respectively.

From 2021 to 2023, he was a Postdoctoral Associate and Faculty Co-advisor Terps Racing EV with the Department of Electrical and Computer Engineering, University of Maryland, College Park, MD, USA. He is currently a Technical Leader with KPIT Technologies GmbH, Munich, Germany. His research interests include areas of high-power converters, drives, and dc–dc converters.

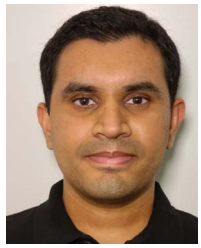

Akshay Singh (Member, IEEE) received the B.Tech. and M.Tech. degrees in electrical engineering from the Indian Institute of Technology, Kharagpur, India, in 2016, and the M.S. and Ph.D. degrees in electrical engineering from the University of Maryland, College Park, MD, USA, in 2020 and 2021, respectively.

He is currently a Staff Power Electronics Engineer with Tesla, Inc., Palo Alto, CA, USA. His current research interests include power electronics for transportation electrification and energy management applications, with a focus on modeling and optimization of compact, high-efficiency dc–dc and ac–dc converters using wide-bandgap devices, and high-frequency magnetics.

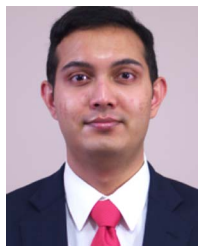

Arafat Hasnain (Student Member, IEEE) received the B.S. and M.S. degrees in electrical engineering from Villanova University, Villanova, PA, USA, in 2017 and 2019, respectively. He is currently working toward the Ph.D. degree in electrical engineering with the University of Maryland, College Park, MD, USA.

His current research interests include the design, and modeling of high-efficiency, compact wide-bandgap based converters, and high-frequency magnetics for applications in transportation electrification and renewable energy integration.

Alireza Khaligh (Senior Member, IEEE) is a Professor and the Director of the Maryland Power Electronics Laboratory (MPEL), Department of Electrical and Computer Engineering (ECE), and the Institute for Systems Research (ISR), University of Maryland, College Park (UMD), MD, USA. He has authored or coauthored more than 220 journal and conference papers. His research interests include modeling, analysis, design, and control of power electronic converters for transportation electrification, renewable energy, and wearable electronics.

Prof. Khaligh was a recipient of various recognitions including 2016 UMD Clark School of Engineering E. Robert Kent Junior Faculty Teaching Award, 2017 UMD Office of Technology Commercialization Overall Invention of the Year Award, 2018 UMD ECE Jimmy Lin Award for Innovation, 2019 UMD ISR Outstanding Systems Engineering Faculty Award, 2020 Nagamori Award, 2022 IEEE PELS Vehicle and Transportation Systems Achievement Award, and 2024 UMD Linda Clement Outstanding Advisor Award, among many others. He was the General Chair of the 2016 IEEE Applied Power Electronic Conference and Expo (APEC), and the General Chair of the 2013 IEEE Transportation Electrification Conference and Expo (ITEC).